Effects of 3D magnetic perturbation on divertor heat load redistribution on ASDEX Upgrade

Y. Gao[1], M. Rack[1], Y. Liang[1], B. Sieglin[2], P. Denner[1], W. Suttrop[2], A. Kirk[3], E. Wolfrum[2], the EUROfusion MST1 Team*, and the ASDEX Upgrade Team

[1] *Forschungszentrum Jülich GmbH, Institut für Energie- und Klimaforschung – Plasmaphysik, 52425 Jülich, Germany*

[2] *Max-Planck-Institut für Plasmaphysik, D-85748 Garching, Germany*

[3] *CCFE, Culham Science Centre, Abingdon, Oxon, OX14 3DB, UK*

For the ITER design, one of the biggest challenges is the power handling with respect to the safety of in-vessel components. The application of magnetic perturbations (MPs) is a promising technique for controlling or optimizing plasma-wall interactions [1]. ASDEX Upgrade is equipped with toroidally distributed in-vessel MP coils (8 above and 8 below the mid-plane), which can perform a rigid rotation or differential phase scan with toroidal mode numbers $n = 1, 2$.

On ASDEX Upgrade, ELM mitigation has been achieved using MPs. In low collisionality experiments ($\nu^*_{\mathrm{ped}} < 0.5$), the MPs have been shown to reduce the heat flux factor [2, Eq. 1] by 75 %, at the cost of an MHD confined energy drop of ~ 30 % [3, 4]. In high collisionality with strong gas puffing, ELM mitigation can be obtained by the change from Type-I to small ELMs [5].

The heat load distribution on the outer divertor plate has been analysed in detail, by means of infra-red (IR) camera measurement with a high spatial resolution of ~ 0.6 mm and a frame rate of ~ 3.3 kHz. In both collisionality regimes, clear splitting of the outer strike line has been observed due to the application of MPs.

Fig. 1 shows the footprints at the target plate of Divertor-III.BG1 during a rigid rotation of an $n = 2$ MP at low collisionality for AUG discharge # 30839. Here, the phase between the field patterns in the upper and lower MP coils has been kept constant ($\Delta\Phi = 0°$, "even" parity). The rotation has been performed with a frequency of 0.5 Hz. Except for the first toroidally symmetric strike line, two additional strike lines on the outer divertor have been observed to move with the rotating MPs. The appearance of these additional strike lines is due to the new channels for particle and energy transport in the magnetic flux tubes generated by the MPs.

In both the two cycles of the rotation with differing heating power (4.8 MW and 7.1 MW), the entire 3D features of the magnetic topology at the plasma edge induced by MPs manifest

*See `http://www.euro-fusionscipub.org/mst1`

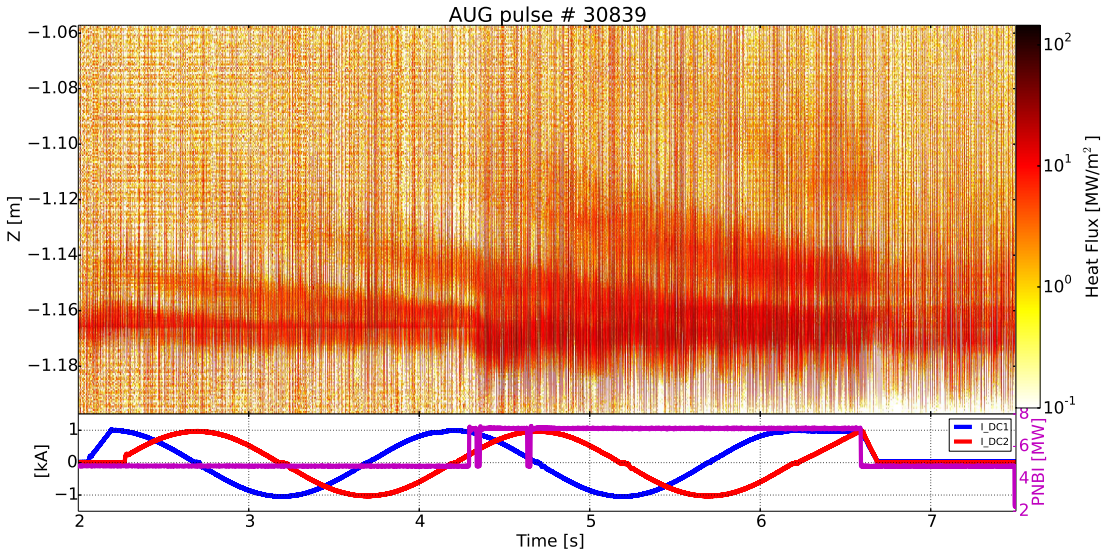

Figure 1: The heat flux map showing the movement of secondary strike lines with rigid rotating MPs. The lower part of the figure are the time evolution of the MP coils currents (blue, red) and NBI power (violet).

themselves as the helically striated divertor footprint patterns. After each cycle of the rotation with constant plasma parameters and IR monitoring at one toroidal angle, the whole toroidal distribution of the heat load can be obtained. The amplitude of the heat flux has been observed to differ at different lobes on the target. It may be due to the different connection length of the field lines in the 3D magnetic lobes intersected by the target plate. This could be modelled and compared with experimental results in the future using field line tracing codes.

In a high collisionality regime, gas puffing scans are performed with the application of MPs. In Fig. 2, the heat flux distribution over time for discharge # 30589 is presented (toroidal magnetic field $B_T = -2.5\,T$ and plasma current $I_P = 800\,kA$). The lower panel shows a ramping up phase of the gas puffing rate within the flattop of MP coil currents. The signal of divertor current I_{div} presented here is used as ELM indicator, which shows the transition of Type-I ELMs to more frequent small ELMs starting at $\sim$ 6.97 s due to the increase of the gas puffing rate. The gas inlet system consists of several valves at different toroidal angles but all fuelling from the lower private flux region. It can be seen obviously that the strike line splitting appears for both low and high gas puffing time periods within the flattop of MPs as shown in Fig. 2. Before the flat-top of MP coil currents, the splitting cannot be seen. After the turning off of MP coil currents, the splitting fades away gradually. This indicates that the MPs modify the edge magnetic topology and generate additional channels for particle and energy transport.

In order to study the gas puffing effect on heat flux redistribution between the first strike line and splitting patterns, two time periods are selected and compared in detail. From 5.705 s to

6.089 s the gas puffing rate is at the constant lowest value of 5×10^{21} D/s, while from 7.238 s to 7.499 s the gas puffing rate is at the constant highest value of 30×10^{21} D/s. In Fig. 3, the two time periods have been zoomed in and analysed in detail. At the low gas puffing rate, 40 Type-I ELMs are identified with crash duration of ~ 3 ms and the peak heat flux up to 85 MW m^{-2}. At

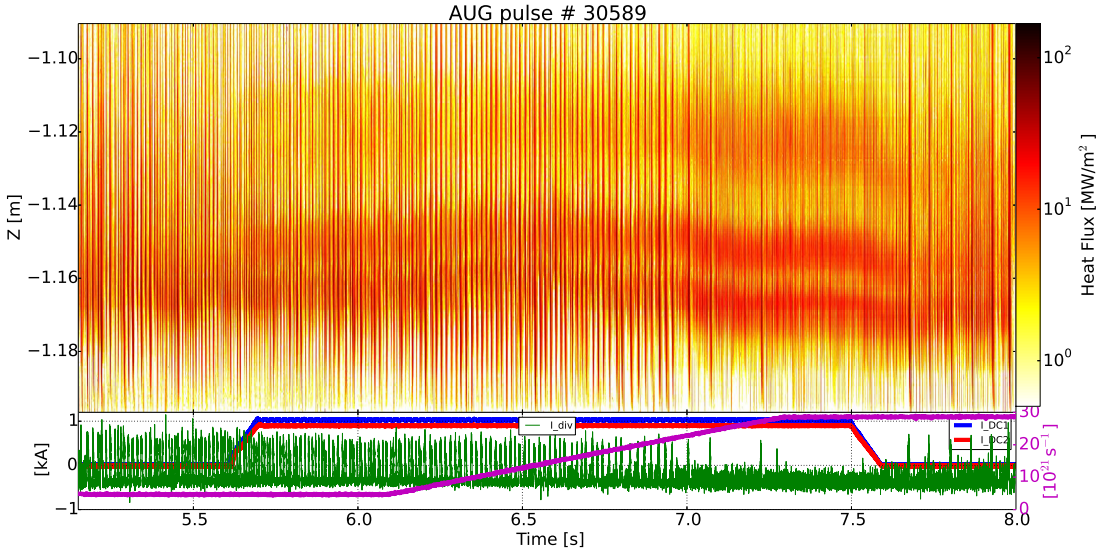

Figure 2: The time evolution of heat flux distribution on the outer target. The lower panel shows the gas puffing rate (violet), the MP coils currents (blue, red) and the dievertor current signal (green).

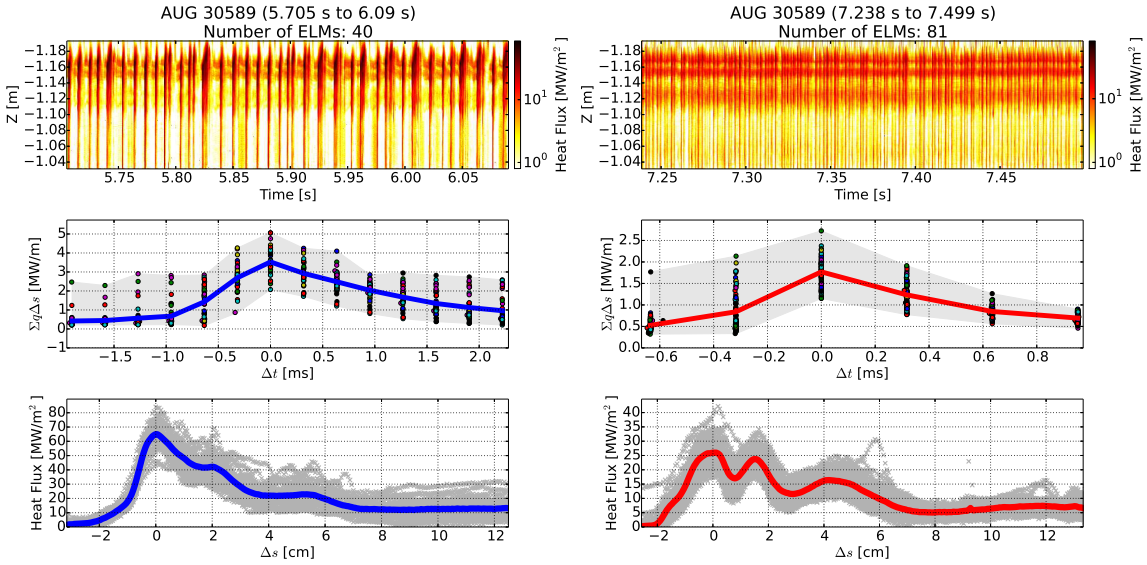

Figure 3: The comparison of the heat flux distribution on the outer target between low (left) and high gas puffing (right). The first row shows the time evolution of the heat flux distribution on the target. The second row shows the spatially integrated heat flux profile with $\Delta t = 0$ referring to the peak ELM crash moment. The bottom row shows the heat flux profiles on the target for every ELM at $\Delta t = 0$ as well as the average of these profiles (bold curve). The Δs is correlated to the first peak.

the high gas puffing rate, 81 small ELMs are detected with power decay time reduced to ~ 1 ms and the peak heat flux lower than 45 MW m^{-2}. In Fig. 4, the comparison of the averaged heat flux profile is presented. All the profiles are normalized to the peak of the ELM crash heat flux profile at the low gas puffing rate. The strike line splitting has be seen in all the profiles. But the distribution of the heat load in different lobes could be modified by the gas puffing rate. With increasing gas puffing the peak heat flux is reduced by 60 % during the ELM crash phase, while the ratio of the secondary to the first peak in the heat flux profile can be enhanced by a factor of 1.8. The averaged pre-ELM profiles are generated using the same phases in the discharge as the ELM crash profiles. During the pre-ELM phase, the heat flux is higher in all the lobes at high gas puffing rate.

At ELM crash phase, the effect of ELM mitigation by gas puffing is obvious because of the reduction of the heat load at the first toroidally symmetric strike line. However the ratio of the secondary to the first heat flux peak is enhanced. The formation of the secondary peaks is considered to be the parallel transport of particles along the perturbed field lines in the flux tubes induced by the MPs. Depend on the penetration depth of the MPs, these perturbed field lines may lead hot particles from confined region to the divertor with short connection length. Another explanation could be the increased perpendicular transport in high collisionality plasma, which could populate more particles into the outer lobes. This result is qualitatively consistent with the observations on EAST, which may provide an attractive approach to actively redistribute the heat load [6].

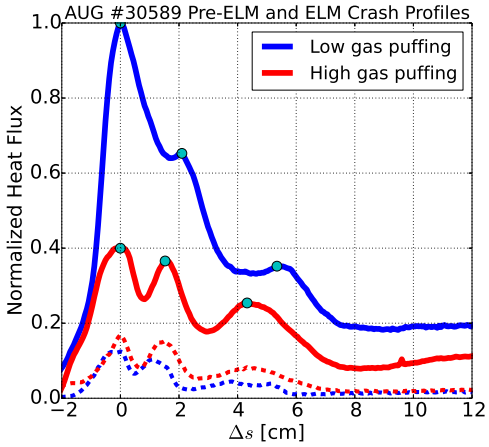

Figure 4: The comparison of averaged heat flux profile between low (blue) and high gas puffing rate (red). The dashed lines are pre-ELM footprints.

Acknowledgement

This work has been carried out within the framework of the EUROfusion Consortium and has received funding from the Euratom research and training programme 2014-2018 under grant agreement No 633053. The views and opinions expressed herein do not necessarily reflect those of the European Commission.

References

[1] A. Loarte *et al. Nuclear Fusion*, **54** (3), 033007 (2014).
[2] A. Herrmann. *Plasma Physics and Controlled Fusion*, **44** (6), 883 (2002).
[3] W. Suttrop *et al.* In *25th IAEA Fusion Energy Conference (FEC 2014)* (2014).
[4] A. Kirk *et al. Nuclear Fusion*, **55** (4), 043011 (2015).
[5] E. Wolfrum *et al.* In *41st EPS Conference on Plasma Physics* (2014).
[6] Y. Gao *et al. Plasma Science and Technology*, **16** (2), 93 (2014).